Proceedings of Global Power and Propulsion Society
ISSN-Nr: 2504-4400
GPPS Xi'an21
18th – 20th October, 2021
www.gpps.global

GPPS-TC-2021-0120

RESEARCH ON THE APPLICATION OF SIMILARITY PRINCIPLE FOR MULTISTAGE AXIAL COMPRESSOR

Hong Xie
Shanghai Jiaotong University
369165499@qq.com
Shanghai, China

Bo Yang
Shanghai Jiaotong University
byang0626@sjtu.edu.cn
Shanghai, China

Shuyi Zhang
Shanghai Jiaotong University
homedown.good@163.com
Shanghai, China

Moru Song
Shanghai Jiaotong University
Summery0624@163.com
Shanghai, China

Guoming Zhu
Shanghai Jiaotong University
1562161048@qq.com
Shanghai, China

ABSTRACT

Low-speed model fabrication is an effective testing method for deep understanding flow characteristics with low cost and low risk, so it is extensively used in design and optimization of high speed and small scale compressors. Reynolds number, Euler number and Strouhal number are demanded to retain constant for exact similarity method. It is nearly impossible in practical application. In this paper, an improved similarity principle is proposed for high-to-low model scaling process based on the comprehensive considerations of geometrical and aerodynamic parameters. Three parameters, *Sr* (Strouhal number), *CFE* (correction friction Euler number) and *DF* (diffusion factor) are determined as the criterion parameters of similarity principle in scaling process. The relative errors of efficiency and pressure ratio at design point of prototype and low-speed model are about 2.4% and 2.1%, respectively. And, the deviation of flow coefficient near stall is about 1.6%. The similar aerodynamic performance and flow fields at design and off-design points are both achieved.

Key words: similarity principle; Reynolds number; Euler number; diffusion factor

INTRODUCTION

The low speed modelling method, based on the ideology of similarity, was first proposed by Wisler [Wisler, 1985]. The experimental study through low-speed model could be used for understanding intricate flow fields [Zhang, 2014] and optimization of prototype [Zhang, et al, 2016]. The same blade surface velocity distribution was the key strategy to obtain low-speed model. In addition, the scaling process needed iterative procedure and repeating-stage [Zhang, 2014]. However, the former method caused some shortages in the practical application inevitably. Firstly, the iterative procedure was time-consuming whether using numerical simulation or experimental methods. And, the repeating-stage was needed in this method, which was high cost and invalid for multistage compressor. Besides, the method ignored some important parameters in flow fields, such as tip clearance, Reynolds number (*Re*), Mach number (*Ma*), etc. Therefore, it is necessary to develop an improved scaling method with the advantages of time-saving, more accurate and wider application.

In recent decades, some researchers focused on dig out the key influence factor to improve the scaling method. The complete flow similarity could be fulfilled when *Ma* and *Re* are maintained according to the study of Asad [Asad, et al, 2003]. The effects of *Ma* and *Re* in the scaling process were theoretically quantified by researchers [Ma and Xi, 2010]. But, it was nearly impossible to maintain *Ma* and *Re* at the same time because of limited dimension and power of test rig. So, the compromise was required in practical application to establish test rig with appropriate geometrical and aerodynamic parameters. One of the options was to retain constant *Re*. Under the same Re conditions, Gonzalez redesigned blade [Gonzalez, et al, 2002] and Marconcini changed blade profile with the help of their low-speed testing [Xie, et al, 2020]. While, the disadvantage of this option was that the fluid compressibility was ignored, resulting not adequately flow similarity. The other option was neglecting the effects of *Re* at the first procedure of scaling process [Casey, 1985]. Then, the flow losses related to *Re* could be compensated [Pelz and Stonjek, 2014] through performance correction or geometric

modification [Xie, et al, 2020]. The feasibility of this option has been proved in some researches [Markus, et al, 2019]. However, most of the researches focused on the correction of performance curves rather than similarity of flow fields. Up to present, there was still not investigation on proposing a scaling principle, which could both achieve similar enough internal flow regimes and operating performance curves.

In this study, new similarity criterions were developed, and a low-speed model was fabricated from a multistage axial compressor with high-speed and small-scale based on this improved method. The scaling method and analysis of the flow fields were validated by numerical simulation.

SCALING METHOD

Geometric structure, dynamic and kinematic similarity are prerequisite for achieving similar flow characteristics between the prototype and low-speed model. One of the methodologies to derive the similarity principle is dimensional analysis based on the Buckingham–PI theorem. Generally, there are 7 variables overall when applying the similarity principle in this investigation, and they are $\rho, u, D, P, T, t,$ and μ. The base dimensions are the length dimension *L*, mass dimension *M* and time dimension *t*. And, ρ, u, D are the base variables. Finally, the flow characteristics are summarized as Equation (1).

$$\begin{cases} F\left(EU, \dfrac{EU}{R}, \dfrac{1}{Sr}, \dfrac{1}{Re}\right) = 0 \\ EU = \dfrac{1}{\kappa}\left(\dfrac{1}{Ma}\right)^2 \\ Ma = \dfrac{\sqrt{\kappa RT}}{u} \\ \mathrm{Re} = \dfrac{\rho u D}{\mu} \\ Sr = \dfrac{D}{ut} \end{cases}, \tag{1}$$

Consequently, the flow similarity principle derived from dimensional analysis can be summarized to be the constant *Eu*, *Eu/R*, *Sr* and *Re*. In this study, the gas constant *R* is unchanged and the variation of the adiabatic index κ is tiny. *Re* is ignored at the beginning and then the effects of *Re* are compensated with some corrections. The fabrication of low-speed model is based on the steady flow parameters, so the *Sr* meaning unsteadiness can be replaced by the flow coefficient ϕ which represents the kinematic similarity under steady condition. The derivation of flow coefficient at design under steady condition is shown on equation (2).

$$\pi_3 = \rho^0 u^1 D^{-1} t = \frac{ut}{D} = \frac{\frac{\pi}{4} D^2 \bullet u}{\frac{\pi}{4} D^2 \bullet \frac{D}{t}} = \frac{\frac{\pi}{4} D^2 \bullet u}{Q} = \frac{1}{\phi}, \tag{2}$$

In this case, the characteristic dimension *D* is set to be the diameter of rotor D_2, the characteristic velocity is u_2, so the characteristic flow coefficient ϕ_{u_2} is calculated as:

$$\phi_{u_2} = \frac{Q}{\pi/4 \cdot u_2 \cdot D_2^{\,2}} \tag{3}$$

In a few words, the scaling method and process could be divided into two procedures. At first, the low-speed model *A* was established based on the identical characteristic flow coefficient and *Eu*. Secondly, some dimensionless aerodynamic parameters and geometric parameters were corrected to offset the *Re* effects. In the correction process, new dimensionless parameters were proposed as correction similarity principle for achieving flow similarity.

NUMERICAL METHOD

The commercial code EURANUS were employed for obtaining the flow fields details by dealing with the conservative R-A(Reynolds-averaged) N-S(Navier-Stokes) equations. The calculation was solved with an explicit four-stage Runge-Kutta method by local time step for convergent solutions. The eddy viscosity in the turbulence simulation was estimated with the S-A(Spalart-Allmaras's) model [Spalart and Allmaras, 1992]. The current model included seven blade rows, and the blades numbers of IGV (inlet guide vane), first stage rotor (*R1*), first stage stator (*S1*), second stage rotor (*R2*), second stage stator (*S2*), third stage rotor (*R3*) and OGV (outlet guide vane) were 73, 93, 99, 93, 99, 97 and 90, respectively. After

grid sensitivity analysis, the ultimate mesh number of single-passage model was about 9 million, balancing the accuracy and computation time. The computation domain and grid details is shown in Fig.1.

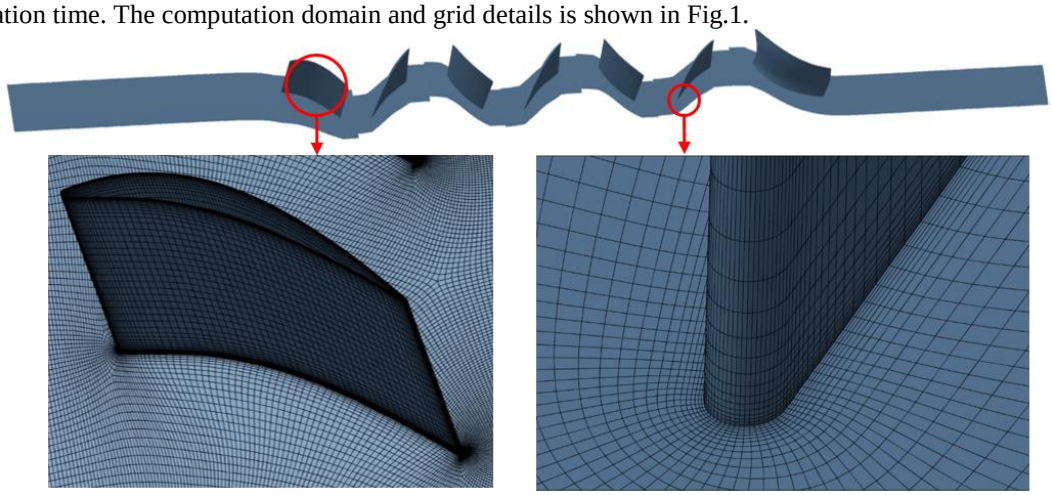

Figure 1 Computation domain and grid details

Considering the consistent frictional forces, all the solid boundaries were set to be no-slip, adiabatic and hydraulically smooth. Under these conditions, the only change brought by geometrical scaling was inertial forces, decreasing the impact parameter on *Re* to one. Velocity direction, total pressure and total temperature were imposed at inlet boundary plane, and average static pressure were imposed at outlet plane. The outlet static pressure was varied gradually to obtain the whole stable operating performance. The last converged point was regard as near stall point in steady calculation.

RESULTS AND ANALYSIS

Comparison of the prototype and low-speed model *A*

The low-speed model A is fabricated from prototype through scaling up geometrically by SF (scaling factor) 1:2. Due to the relatively tiny size of tip clearance, the momentum flux leaving the tip gap is relatively small and can be ignored at the first step of scaling process. So, the drag force per unit depth, which is proportional to $\rho U_0^2 l_0$ according to the theorem of momentum, can be expressed as [Cameron, et al, 2013]:

$$F_x \propto \rho U_0^2 \propto \rho U_j^2 h \tag{4}$$

which can be simplified as

$$\frac{l_0}{h} \propto \left(\frac{U_j}{U_0}\right)^2 \tag{5}$$

where, F_x represents the axial drag force, U_0 the free-stream velocity, U_j the wall jet velocity, h the tip clearance height, l_0 the distance from the start of leakage flow to the interface of leakage and main flow. And, the equation (16) can be changed to be equation (17) based on the leakage model of Chen [Yu, 2017].

$$\frac{l_0}{c_{ax}} \propto \frac{h}{c_{ax}} \times \left(\frac{U_j}{U_0}\right)^2 = \frac{h}{c_{ax}} \times \frac{1}{\phi^2} \times \left(C_{ps} - C_{ss}\right) \tag{6}$$

where, c_{ax} is the axial chord length, C_{ps} the pressure coefficient of pressure side and C_{ss} the pressure coefficient of suction side. As depicted in equation (17), the same ratio of tip clearance height and axial chord length h/c_{ax} can assure the similar tip leakage flow structures. So, the ratios h/c_{ax} of model *A*, *B* and *C* are set to be the same as that of prototype . The inlet boundary conditions are varied in line with the method of first step in scaling procedures. The inlet flow coefficient and *Eu* are retained constant, yielding small change of *Ma* and obvious change of *Re*. The geometric and aerodynamic parameters of the two models are listed in Table 1. Performance comparisons between prototype and model *A* are depicted as function of flow coefficient in Fig.2.

Table 1. Design parameters of prototype and compressor *A*

Parameters	Unit	Value(Prototype)	Value(Model *A*)
Inlet total pressure, P_0	kPa	1753.5	101.3
Inlet total temperature, T_0	K	673	293.15
Design flow coefficient, ϕ_{u_2}		0.0785	0.0785
Characteristic diameter, D_2	mm	550	1100
Tip clearance, h	mm	0.5	1.0
Characteristic blade chord length, b	mm	14	28
Design rotational speed, N	rpm	12000	3960

Peripheral velocity, u_2	m/s	345.4	228
Euler number, *Eu*	-	1.62	1.62
Mach number, *Ma*		0.671	0.664
Reynolds number, *Re*		1.31E+06	4.27E+05
Adiabatic index, κ	-	1.3712	1.402
Working fluid	-	air	air

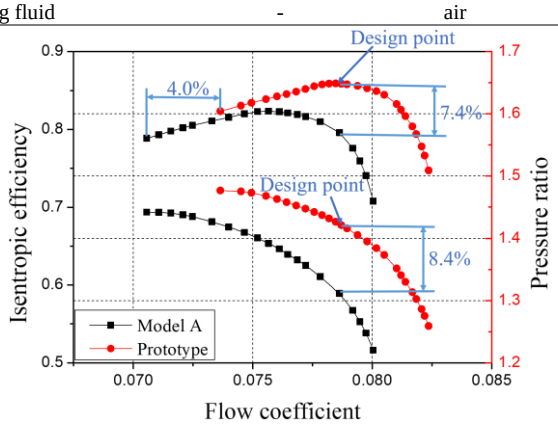

Figure 2 Performance comparison between prototype and mode *A*

The overall trend of the curves matches well between prototype and model *A*. On design point of prototype and the same flow coefficient point of model *A*, the relative deviations of isentropic efficiency and pressure ratio are about 7.4% and 8.4%. And, the relative errors of the flow coefficient near stall is about 4%. It is shown that the aerodynamic performance is deteriorated and the curves are shifted towards to low flow coefficient when the prototype is scaled-up. The explanation for the performance deterioration and change has been introduced in the research of Casey [Casey and Robinson, 2011], which illustrates that one of the main elements is the varied friction factor caused by the changed *Re*. Some recent approaches quantifying the effect of *Re* have been developed, and the concise correction formulas have been summarized [[Markus, et al, 2019]. In this case, the *Re* of model *A* is decreased apparently in scaling process, and the friction factor is increased accordingly. The model *A* shows lower efficiency and the curves migrates to low flow direction is largely due to the decreasing *Re*. So, the correction procedure to achieve similar performance curves and flow fields is the main contents in the following sections.

Correction procedures

Correction of rotation speed

The first step is to correct the end-wall loss according to Fanning equation which is a linear function of Darcy friction factor (D_f) [Mcgovern, 2011]. The D_f can be solved from Colebrook-White formula as [Tefaruk and Mehmet, 2004]:

$$D_f^{-0.5} + 2\log_{10}\left\{e/3.7 + \left(2.51/\mathrm{Re}\right)D_f^{-0.5}\right\} = 0 \tag{7}$$

where, *e* is the relative surface roughness. In this study, the surface is assumed to be smooth, so the *e* can be neglected. Then, equation (11) can be manipulated as:

$$D_f = \left\{-1.15/\ln\left[\left(2.51/\mathrm{Re}\right)D_f^{-0.5}\right]\right\}^2 \tag{8}$$

Iteration method is used conveniently to solve equation (12), and the initial value of D_f is set to be 0.1. The D_f value can be converged within 9 iterations, and the value of model *A* is larger.

The Fanning equation used to estimate end-wall loss *LDF* is described as [Mcgovern, 2011]:

$$LDF = D_f\left(\frac{L}{D}\frac{u_2^2}{2g}\right) \tag{9}$$

The variation of D_f caused by varied Re results in different ratio of end-wall loss and the whole loss (*LDF*/*W*) in scaling process. The peripheral speed u_2, the only parameter can be corrected in this case, should be changed to realize the similar end-wall loss ratio. Substituting the two D_f value into equation (9), and the corrected peripheral speed can be obtained based on the identical *LDF*. The rotation speed is increased to 4356rpm resulted from the corrected u_2, and the model with increased rotation speed is namely model *B*. The corrected u_2 causes the correction of *Eu* according to equation (4), so the *Eu* in the similarity principle is replaced with a new parameter $\lambda \cdot Eu$, where, λ is the reciprocal of D_f for corresponding model. In this study, the new criterion parameter $\lambda \cdot Eu$ is namely *CFE* (correction friction Euler number). Besides, the rotation speed 4356rpm is not the final result of model *B*, because the *Re* is varied when u_2 is increased and the D_f is also changed accordingly. The computation process of D_f and u_2 is also an iterative computing process, and the converged u_2 of model *B* is about 4320rpm. The comparisons of performance curves are shown in Fig.3.

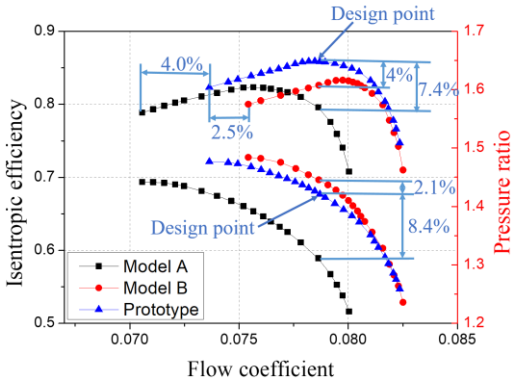

Figure 3 Performance comparison among prototype, model *A* and model *B*

The whole aerodynamic performance is increased with corrected rotation speed. The curves of model *B* match the curves of prototype much better than that of model *A*. The relative errors of efficiency and pressure ratio on design point are decreased from 7.4% to 4% and from 8.4% to 2.1%, respectively. The efficiency of model *B* is still lower than that of prototype, yet the pressure appears the opposite results. The lower efficiency may be caused by the worse flow fields as the increasing blade loading of model *B*, and the higher pressure ratio is the results of larger energy head. In view of not similar enough performance curves, further flow fields analysis and related correction are necessary.

Correction of blade exit angle

The blade profile loss caused by excessive blade loading is closely relevant with diffusion factor (*DF*). *DF* is a significant aerodynamic parameter which represents the blade loading and the ability of pressure rise. And, *DF* has been proved to be an important factor in low-speed model design [Zhang, et al, 2014], so *DF* is also needed to be constant between prototype and low-speed model. *DF* is varied as changed *Re* during scaling process [Bra and Niehuis, 2016], so *DF* of low-speed model needs to be corrected. The *DF* of rotor DF_R can be described as [Lieblein, et al, 1953]:

$$DF_R = 1 - \frac{w_2}{w_1} + \frac{\Delta w_u}{2 w_1 \tau} \tag{10}$$

In this case, the solidity τ is constant because of the exactly geometrical scaling, so the sufficient conditions of consistent DF_R are the constant w_2/w_1 and $\Delta w_u/w_1$. The deduction to achieve the same velocity ratio can be derived from the sketch map of inlet and outlet velocity triangle, as shown in Fig.4. It can be inferred from Fig.4 that when u, β_1, c_{1a}/u are determined the inlet velocity triangle is fixed, and when β_2, c_{2a}/c_{1a} are determined outlet velocity triangle are also fixed. As a result, the w_2/w_1 and $\Delta w_u/w_1$ can retain constant. In this study, the inlet velocity triangle is determined in design, and the consistent flow coefficient guarantees the similar inlet velocity triangle. As mentioned above, the errors of pressure ratio between prototype and low-speed model are relatively small, resulting subtle variation of c_{2a}/c_{1a} in scaling process. It means that the value of c_{2a}/c_{1a} can assumed to be constant in scaling process. So, the only parameter needed to be constant is the outlet flow angle β_2. The constant value of c_{2a}/c_{1a} and β_2 not only ensures the similar outlet velocity triangle, but the identical w_2/w_1 and $\Delta w_u/w_1$.

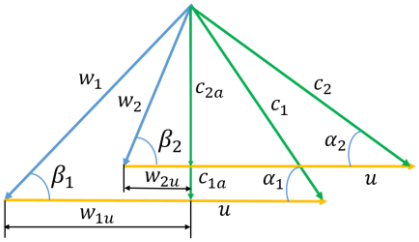

Figure 4 Sketch map of velocity triangle

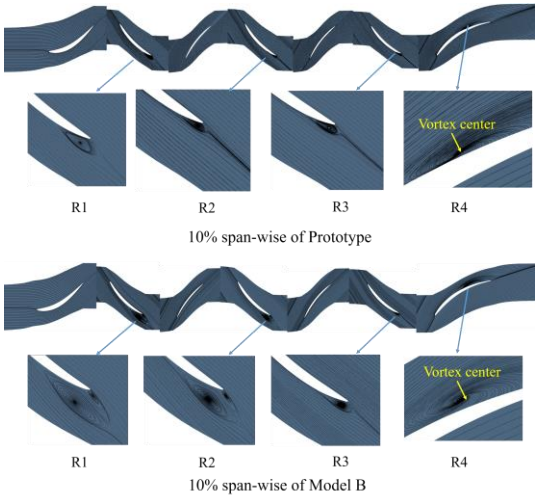

Figure 5 Comparisons of limiting streamlines of prototype and model *B*

The limiting streamlines distributions at 10% span-wise along the blade height of prototype and model *B* on design point are shown in Fig.5. The main flow structures are similar on the whole. There is no obvious difference of the flow streamlines around stators, while the flow separation region near rotor trailing edge of of model *B* is a little larger, especially for *R1* and *R2*. The vortex discrepancy of *R3* is not obviously as in *R1* and *R2*. It may because the effects of *Re* is decreased as the *Re* is increased when fluid flows towards downstream, resulting smaller flow fields difference between prototype and mode *B*. Since the main distinction exists around *R1* and *R2*, the *DF* correction is focused on *R1* and *R2*.

The outlet flow angle β_2 is adjusted by changing the outlet blade angle, which is conducted in the Auto-Blade modular of NUMECA [Numeca, 2017]. Since different distributions of β_2 mainly emerge from blade root to 30% blade height, so three sections (0%, 15% and 30% blade height, respectively) are adopted for the geometrical revision. The blade shape near trailing edge is adjusted until the aerodynamic agreement is satisfied between prototype and model *C*. The outlet blade angle of low-speed model is decreased, and the geometrical comparison between model *B* and *C* is shown in Fig.6. The outlet blade angel is changed biggest at 0% blade height, then the 15% and smallest at 30% blade height. Outlet flow angle distributions of *R1* and *R2* among prototype, model *B* and the revised model C are compared in Fig.7. The β_2 of model C matched relatively well with prototype, although small errors exist near blade tip.

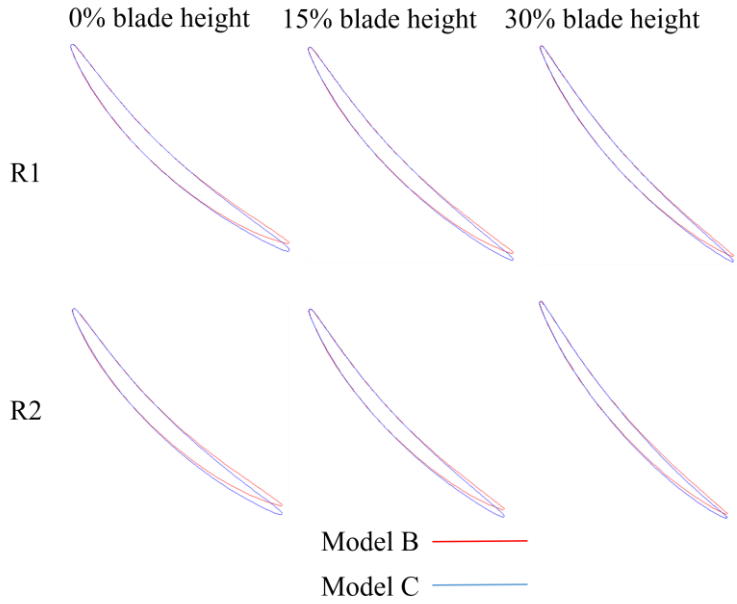

Figure 6 The profiles of model B and C

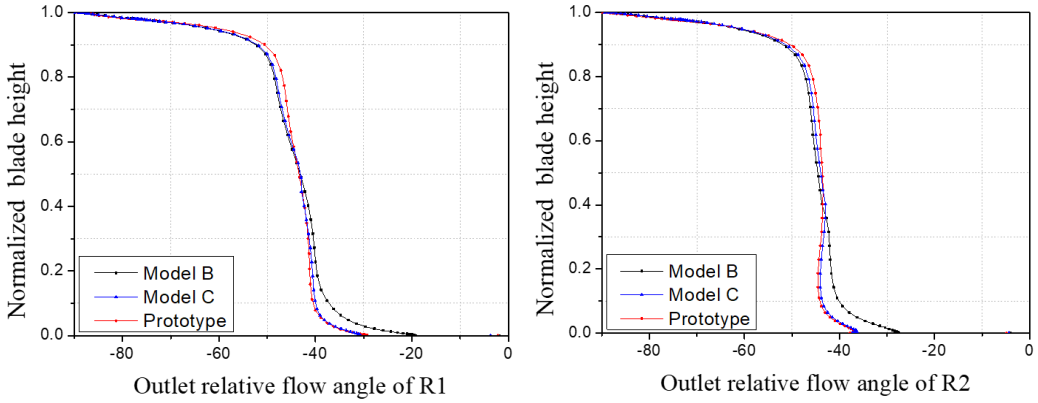

Figure 7 Comparisons of outlet relative flow angle

The limiting streamlines distributions on suction surfaces and axial velocity coefficient (ratio of axial velocity to peripheral velocity) among prototype, model *B* and *C* at design point are shown in Fig.8. The secondary flow emerges in the hub corner and mitigates towards the blade tip. The separation line occurred at the junction position where the axial velocity gradient changes greatly near the suction surface. The separation region of model *B* is apparently larger than prototype. At the hub, separation domain of model *B* occupies about 60% chord-wise length of *R1* and about 50%of *R2*, respectively, compared to 45% and 30% of prototype. One of the reasons for larger separation for model *B* is because of thicker boundary layer caused by lower velocity and lower *Re*. And, more momentum loss further promotes separation formation and then brings about more serious separation. The wake vortex (marked with red circle) exists in three models near trailing edge of *R1* and *R2*, yet the vortex intensity of model *B* is strongest. There is only one obvious vortex appears near the junction of hub and suction surface of *R1* for prototype, while two vortexes appear for model *B* and vortexes

intensity is increased. In addition, two vortexes also appear near the junction position of *R2* for model, while there is no obvious vortex for prototype. The pressure difference is formed at separation area of hub where the low energy and velocity flow with high static pressure meets main flow. Under the effects of negative pressure gradient, the low energy flow migrates towards the blade tip. So, another reason for larger separation near suction surface for mode *B* is that the more intense separation at hub facilitate more serious separation, resulting in more efficiency loss. The excessive blade loading maybe the third reason for the larger separation of model *B*, which can be inferred from the higher pressure ratio, as shown in Fig.3. The oversized outlet blade angle causes exceeding β_2 which produces excessive blade loading, resulting large flow separation.

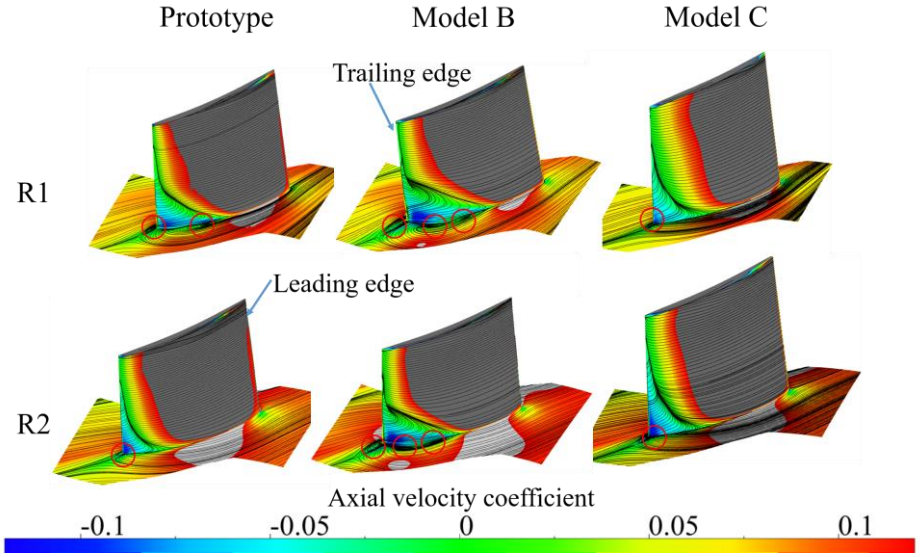

Figure 8 Comparisons of flow fields among prototype, model *B* and model *C*

As a result, the decreased outlet blade angle reduces the blade loading, which relieves the separation near the blade suction surface, and leads to similar β_2 and *DF*. The distributions of axial velocity in Fig.8 can be used to estimate the influence of outlet blade angle. Compared to model *B*, axial velocity at hub corner of model *C* increases obviously, reducing the separation of suction surface and hub corner. The number of the vortexes is reduced to the same as prototype, and the intensity is also weakened to be similar. And, the separation line of model *C* occupies similar area as prototype. In summary, the flow characteristics of model *C* are further similar as prototype through achieving similar *DF* by adjusting outlet blade angle. The performance at off-design points can be seen in Fig.9. For model C, the efficiency is increased because of the decreased separation, while the pressure ratio is reduced because of the adjusted outlet blade angle. The reduced turning angle represents lower blade loading and *DF*, which results in lower pressure rise of model *C*. Simultaneously, the flow blockage is also reduced, causing the near stall flow coefficient move towards low flowrate. The relative errors of efficiency and pressure ratio between prototype and model *C* are about 2.4% and 2.5%, respectively. The error of near stall flowrate is reduced to 1.6%. Moreover, the whole performance curves of mode*l C* match better with prototype than model *B*.

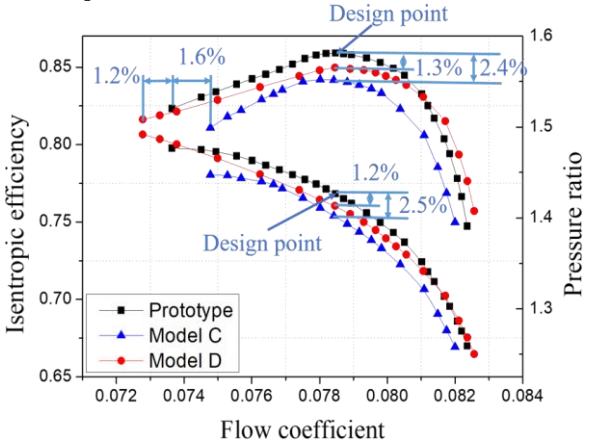

Figure 9 Performance comparison among prototype, model *B* and model *C*

DISCUSSIONS

The fabrication of low-speed model applied by the former researchers is based on the key how to map the low-speed blade loading to high speed, and this method has been proved to be reliable. Due to the reason that the methodology exists some inevitable shortages, a new principle is proposed in this paper. The Ma is maintained and the Re is replaced with

some correction principle. Considering the limitation of the length of the paper, some investigation results will be presented in the future article, such as the investigation on compressibility effects, unsteady effects and the tip clearance on stall margin. Moreover, the test rig is established in Shanghai Jiaotong University and the experiment is carrying out for the validation and the measurement results will be also present in the future research.

CONCLUSIONS

- The exact similarity principle is deduced according to the dimensional analysis based on the similarity requirements of geometric structure, dynamic and kinematic. The maintain of *Re*, *Eu* and *Sr* is necessary for the flow similarity. For the practical application, the exact similarity principle is improved. The achievement of flow similarity base on the improved similarity principle is divided into two procedures. The *Eu* and ϕ are retain constant at the first step to fabricate the low-speed model *A*. And, the second procedure is to optimize the flow similarity by compensating the effects of Re, which are ignored in the first step.
- Three dimensionless parameters, *CFE* and *DF* are proposed as the supplementary criterion to improve the similarity principle. *CFE* is used for effects correction of *Re* on friction loss with corrected rotational speed, and *DF* is employed for correction of blade loading with corrected outlet flow angle. The efficiency and pressure ratio errors at design point between prototype and low-speed are decreased to be 2.4% and 2.1%, respectively. Moreover, the performance curves and flow fields are getting more and more similar with the application of similar *CFE* and *DF*.

Funding: This research was funded by the National Science and Technology Major Project (2017-V-0012-0064).

NOMENCLATURE

c	=	absolute velocity (m/s)
P	=	Pressure (KPa)
Q	=	Volume flow rate (m^3/s)
T	=	Temperature (K)
W	=	The whole loss(J/kg)
t	=	Time (s)
u	=	Velocity (m/s)
w	=	Relative velocity (m/s)
ρ	=	Density (kg/m^3)
μ	=	Dynamic viscosity ($N \cdot S/m^2$)

SUBSCRIPTS

1	=	Inlet of rotor
2	=	Outlet of rotor
p	=	Pressure side
s	=	Suction side
m	=	Low-speed model
i	=	prototype

REFERENCES

1. Wisler, D.C. (1985). Loss Reduction in Axial-Flow Compressor Through Low-Speed Model Testing. *ASME Journal of Engineering for Gas Turbines and Power*, 107(2), pp.354-363. DOI:10.1115/1.3239730.
2. Vera, M., Zhang, X.F., and Hodson, H.P. (2007). Separation and Transition Control on an Aft-Loaded Ultra-High-Lift LP Turbine Blade at Low Reynolds Numbers: High-Speed Validation. *ASME Journal of Turbomachinery*, 129(2), pp.340-347. DOI:10.1115/1.2187524.
3. Zhang, C.K.; Hu, J., Wang, Z.Q., and Li, J. (2016). Experimental Investigations on Three-Dimensional Blading Optimization for Low-Speed Model Testing. *ASME Journal of Engineering for Gas Turbines and Power*, 138(12), pp.122602 (12 pages). DOI:10.1115/1.4033940.
4. Zhang, C.K., Hu, J., Wang, Z.Q., and Gao, X. (2014). Design Work of a Compressor Stage Through High-To-Low Speed Compressor Transformation. *ASME Journal of Engineering for Gas Turbines and Power*, 136(6), pp.064501 (7 pages). DOI:10.1115/1.4026520.
5. Asad, M.S., William, K., George, W. K., and Jr. (2003). Reconsideration of the Fan Scaling Laws: Part I—Theory. *In Proceedings of the ASME/JSME 2003 4th Joint Fluids Summer Engineering Conference*, Honolulu, HI, USA, 6–10 July 2003; ASME Paper No. FEDSM2003-45414, pp. 1307–1315, DOI:10.1115/FEDSM2003-45414.
6. Ma, Y., and Xi, G. (2010). Effects of Reynolds Number and Heat Transfer on Scaling of a Centrifugal Compressor Impeller. *In Proceedings of the ASME, Turbo Expo: Power for Land, Sea, and Air*, Glasgow, UK, 14–18 June 2010; ASME Paper No. GT2010-23372, pp. 565–572, DOI:10.1115/GT2010-23372.
7. Gonzalez, P., Ulizar I., Vazquez R., and Hondson, H.P. (2002), Pressure and Suction Surfaces Redsign for High-Lift Low-Pressur Turbines. *AMSE Journal of Turbomachinery*, 124(2), pp.161-166.DOI:10.1115/1.1452747.
8. Xie H., Song M.R., and Yang B. (2021). Research on the Application of Partial Similarity for a 1-1/2 Axial Compressor. *Processes*, 8(9), pp.1121. DOI:10.3390/pr8091121.

9. Casey M.V. (1985). The effects of Reynolds Number on the Efficiency of Centrifugal Compressor Stages. *ASME Journal of Engineering for Gas Turbines and Power*, 107(2), pp.541-548. DOI:10.1115/1.3239767.
10. Pelz P.F., and Stonjek S.S. (2014). Introduction of an Universal Scale up Method for the Efficiency of Axial and Centrifugal Fans. *In Proceedings of the ASME, Turbo Expo: Power for Land, Sea, and Air*, Dusseldorf, Germany,16-20 June 2014; ASME paper No:GT2014-25403, pp. V01AT10A007(11 pages). DOI:101.1115/GT214-25403.
11. Xie, H., Yang, B., Zhang, S., and Song, M. (2020). Performance Analysis and Improvement of a Centrifugal Compressor Based on Partial Similarity Principle. *ASME Journal of Engineering for Gas Turbines and Power*, 142(5), pp.05012 (12 pages). DOI:10.1115/1.4046925.
12. Markus D., Christoph S., and Jurg S. (2020). The Role of Reynolds Number Effect and Tip leakage in compressor Geometry Scaling at Low Turbulent Reynolds Number. *ASME journal of Turbomachinery*, 142(3), pp.031003(11 pages). DOI:10.1115/1.4045465
13. Spalart, P.R., and Allmaras, S.R. (1992). A one equation turbulence model for aerodynamic flows. *In Proceedings of the 30th Aerospace Sciences Meeting and Exhibit*, Reno, NV, USA, 6–9 January 1992, AIAA paper, DOI:10.2514/6.1992-439.
14. Cameron J.D., Bennington M.H., Ross M.H., Morris S.C., Du J., Lin F., and Chen J.Y. (2013). The Influence of Tip Clearance Momentum Flux on Stall Inception in a High-Speed Axial Compressor. *ASME Journal of Turbomachinery*, 135(5), pp.051005(11 pages). DOI:10.1115/1.4007800.
15. Chenghai, Y. (2017). *Application of the Low-Speed Similitude Modeling Principle in Highly Loaded Axial Compressor Design*. Ph.D. Universigy of Chinese Academy of Sciences.
16. Casey M.V., and Robinson C.J. (2011). A unified correction method for Reynolds number, size, and roughness effects on the performance of compressors. *Proceedings of the Institution of Mechanical Engineers, Part A: Journal of Power and Energy*, 225(7), pp.864-876. DOI:10.1177/0957650911410161.
17. Mcgovern J. (2011). *Technical Note: Friction Factor Diagrams for Pipe Flow*. Dublin Institute of Technology.
18. Tefaruk H., and Mehmet A. (2004). Numerical modeling of Darcy-Weisbach friction factor and branching pipes problem. *Advanced in Engineering Software*, 35(12), pp. 773-779. DOI: 10.1016/j.advengsoft.2004.07.005.
19. Zhang C.K., Hu J., and Wang Z.Q. (2014). Investigations on the Effects of Inflow Condition and Tip Clearance Size to the Performance of a Compressor Rotor. *ASME Journal of Engineering for Gas Turbines and Power*, 136(12), pp: 122608(9 pages). DOI:10.1115/1.4027906.
20. Bra chmanski R., and Niehuis R. (2016). About the Distribution of the Mach Number and Losses Under Consideration of the Diffusion Factor: Profile Distribution and Losses for Low Pressure Turbine Profiles With High Diffusion Factors Under Steady Flow Conditions. *In Proceedings of the ASME, Turbo Expo: Power for Land, Sea, and Air*, Seoul, South Korea. 13-17 June 2016; ASME Paper No: GT2016-57750, pp. V02BT38A054 (13pages). DOI: 10.1115/GT2016-57750
21. Lieblein S., Schwenk F.C., and Broderick R.L. (1953). Diffusion factor for estimating losses and limiting blade loadings in axial-flow-compressor blade elements. *Technical Report. NASA RM E53D01*, Lewis Flight Propulsion Laboratory, Cleveland, Ohio, USA.
22. Numeca. (2017). *Numeca FINETurbo User Guide, Version 11.1*; NUMECA: Beijing, China.